2018-11

A spectrometer for ultrashort gamma-ray pulses with photon energies greater than 10 MeV.

Behm, KT

http://hdl.handle.net/10026.1/13180

A spectrometer for ultrashort gamma-ray pulses with photon energies greater than 10 MeV

K. T. Behm, J. M. Cole, A. S. Joglekar, E. Gerstmayr, J. C. Wood, C. D. Baird, T. G. Blackburn, M. Duff, C. Harvey, A. Ilderton, S. Kuschel, S. P. D. Mangles, M. Marklund, P. McKenna, C. D. Murphy, Z. Najmudin, K. Poder, C. P. Ridgers, G. Sarri, G. M. Samarin, D. Symes, J. Warwick, M. Zepf, K. Krushelnick, and A. G. R. Thomas

Articles you may be interested in

Angular streaking of betatron X-rays in a transverse density gradient laser-wakefield accelerator
Physics of Plasmas **25**, 113105 (2018); 10.1063/1.5054807

Time and position sensitive photon detector for coincidence measurements in the keV energy range
Review of Scientific Instruments **89**, 113101 (2018); 10.1063/1.5048366

Control of quasi-monoenergetic electron beams from laser-plasma accelerators with adjustable shock density profile
Physics of Plasmas **25**, 043107 (2018); 10.1063/1.5023694

Velocity distributions in microskimmer supersonic expansion helium beams: High precision measurements and modeling
Review of Scientific Instruments **89**, 113301 (2018); 10.1063/1.5044203

Femtosecond laser-based phase-shifting interferometry for optical surface measurement
Review of Scientific Instruments **89**, 113105 (2018); 10.1063/1.5057400

Singly charged ion source designed using three-dimensional particle-in-cell method
Review of Scientific Instruments **89**, 113302 (2018); 10.1063/1.5049401

A spectrometer for ultrashort gamma-ray pulses with photon energies greater than 10 MeV

K. T. Behm,[1] J. M. Cole,[2] A. S. Joglekar,[3,4] E. Gerstmayr,[2] J. C. Wood,[2] C. D. Baird,[5] T. G. Blackburn,[6] M. Duff,[7] C. Harvey,[6] A. Ilderton,[6,8] S. Kuschel,[9] S. P. D. Mangles,[2] M. Marklund,[6] P. McKenna,[7] C. D. Murphy,[5] Z. Najmudin,[2] K. Poder,[2] C. P. Ridgers,[5] G. Sarri,[10] G. M. Samarin,[10] D. Symes,[11] J. Warwick,[10] M. Zepf,[9,10] K. Krushelnick,[1] and A. G. R. Thomas[1,12,a]

[1]*Center for Ultrafast Optical Science, University of Michigan, Ann Arbor, Michigan 48109-2099, USA*
[2]*The John Adams Institute for Accelerator Science, Imperial College London, London SW7 2AZ, United Kingdom*
[3]*Physics and Astronomy, University of California, Los Angeles, Los Angeles, California 90095, USA*
[4]*Electrical Engineering, University of California, Los Angeles, Los Angeles, California 90095, USA*
[5]*York Plasma Institute, Department of Physics, University of York, York YO10 5DD, United Kingdom*
[6]*Department of Physics, Chalmers University of Technology, SE-41296 Gothenburg, Sweden*
[7]*SUPA Department of Physics, University of Strathclyde, Glasgow G4 0NG, United Kingdom*
[8]*Centre for Mathematical Sciences, Plymouth University, Plymouth, United Kingdom*
[9]*Institut für Optik und Quantenelektronik, Friedrich-Schiller-Universität, 07743 Jena, Germany*
[10]*School of Mathematics and Physics, The Queen's University of Belfast, BT7 1NN Belfast, United Kingdom*
[11]*Central Laser Facility, Rutherford Appleton Laboratory, Didcot OX11 0QX, United Kingdom*
[12]*Physics Department, Lancaster University, Bailrigg, Lancaster LA1 4YW, United Kingdom*

We present a design for a pixelated scintillator based gamma-ray spectrometer for non-linear inverse Compton scattering experiments. By colliding a laser wakefield accelerated electron beam with a tightly focused, intense laser pulse, gamma-ray photons up to 100 MeV energies and with few femtosecond duration may be produced. To measure the energy spectrum and angular distribution, a 33×47 array of cesium-iodide crystals was oriented such that the 47 crystal length axis was parallel to the gamma-ray beam and the 33 crystal length axis was oriented in the vertical direction. Using an iterative deconvolution method similar to the YOGI code, modeling of the scintillator response using GEANT4 and fitting to a quantum Monte Carlo calculated photon spectrum, we are able to extract the gamma ray spectra generated by the inverse Compton interaction. *Published by AIP Publishing.*
https://doi.org/10.1063/1.5056248

I. INTRODUCTION

Since the first observations of quasimonoenergetic electron beams generated by laser wakefield acceleration (LWFA),[1–3] one application of such beams that has been vigorously researched is for drivers of compact, high-energy photon sources.[4] Inverse-Compton scattering as a laboratory tool has been a useful technique for decades;[5,6] however, it has only been recently that technology has progressed to the point that high power lasers can be used to generate MeV-level gamma rays through inverse Compton scattering using LWFA generated electrons.[7–10] It is desirable to study the creation of bright, multi-MeV photons from a laser-plasma source because they have the potential to be smaller and cheaper than conventional accelerator technology. One of the challenges of using these large devices for real-world applications such as cancer radiotherapy,[11,12] radiography of dense objects,[6,13] isotope identification by nuclear resonant fluorescence,[14] and active interrogation for homeland security[15,16] is that every material being investigated must be brought to one of the few facilities worldwide. Development of an all-optical source opens the door for a greater degree of location flexibility while still having a tunable photon source.

While some applications require inverse Compton scattering in the linear regime, nonlinear inverse Compton scattering experiments can serve to provide an empirical foundation to the physics that govern strong-field quantum electrodynamic (QED) phenomena such as radiation reaction[17,18] or electron-positron pair cascades.[19,20] In our recent experiments,[21,22] a relativistic electron beam produced by laser wakefield acceleration was collided with a counter-propagating laser having a peak focused intensity exceeding 10^{21} W cm^{-2}. The goal was to measure the radiation reaction of the electron beam due to the extreme acceleration it was subjected to at the focus of the intense laser pulse. Measurement of the gamma ray spectrum provides important information for correlating with the electron signal.

There are numerous standard methods for the detection of such high-energy photons, including gas detectors, scintillators, and solid state detectors.[23] Other detection methods for very high energy photons are Cherenkov radiation[24] or Compton scattering and pair creation.[25] For spectroscopy applications, all of these detectors work on the principle that the signal registered is proportional to the energy deposited in the detector such that if a single photon is measured at a time, a photon spectrum may be built up over many measurements. For spectroscopy of high energy photons from laser plasma interactions, for example, in non-linear inverse Compton

---

a)Electronic mail: agrt@umich.edu

scattering experiments, one issue is that the photons are generated in a pulse that is much shorter than the detector time resolution. This means that obtaining a spectrum in a single shot is more challenging. One proposed method is to use Compton scattering, which essentially converts the photon spectrum into an electron spectrum that may be measured by magnetic deflection.[26] Here, we describe the use of a cesium iodide (CsI) crystal array as a primary diagnostic for detection of gamma ray photons in this work and its analysis. A description of the radiation reaction measurement and analysis using the methods described in this paper can be found in the work of Cole *et al.*[21]

II. METHODS

This section details the various techniques employed in calculating a gamma ray spectrum in this inverse Compton scattering experiment. The experimental setup is covered as well as the analysis methods for converting the data into reliable spectra.

A. Experimental setup

This work was carried out on the twin-beam Astra-Gemini laser system at the Rutherford Appleton Laboratory in the UK. Both beam lines were used in this work; one of the pulses was collided with a relativistic electron beam produced by the second laser pulse. The "south" beam line was focused to the edge of a 15 mm diameter gas jet using an $f/40$ spherical mirror to a peak intensity of $I = (7.7 \pm 0.4) \times 10^{18}$ W/cm^2. This beam drove plasma waves through the gas target produced by the 15 mm nozzle, resulting in the acceleration of electrons up to 1 GeV. The "north" beam line was focused to the opposite edge of the 15 mm nozzle by an $f/2$ off-axis parabola reaching a peak intensity of $(1.3 \pm 0.1) \times 10^{21}$ W/cm^2 to collide head-on with the relativistic electron beam. A schematic of the experimental setup is presented in Fig. 1. The spatial overlap of the electron beam with the scattering beam was optimized by performing a raster scan of the scattering beam and measuring the signal in the gamma ray detector.

The gamma rays that were produced by the strong oscillations of the electrons in the intense electric field of the counter-propagating laser were measured using a CsI(Tl) crystal array detector that was housed in a lead enclosure with a 15 mm diameter aperture, as in Fig. 1. Examples of the electron beams and the corresponding CsI gamma-ray signal can be found in Figs. 2 and 4 of the radiation reaction paper by Cole *et al.*[21] The detector consists of 1551 CsI(Tl) crystals arranged in a 47×33 lattice, though only 33 crystals of

penetration depth were captured on the camera, as shown in Fig. 2. The crystals are rectangular prisms that are 5 mm square in cross section and 50 mm in length. The individual crystals are held in place by 1.0 mm thick aluminum spacers that fit together in a matrix pattern inside the housing to support the crystals.

The gamma ray beam was incident on the side of the 9 mm thick steel housing such that the 47 crystals were oriented along the propagation direction and the 33 crystals were oriented in the transverse direction. In order to limit background photons from hitting the CsI detector, it was surrounded by lead bricks. The light output of the crystal lattice was imaged using a 16-bit CCD camera with an objective lens so that the penetration depth and vertical divergence of the beam could be measured on each shot, as shown in Fig. 2. The resulting data file is a 1024×1024 pixelated image of the light output of the CsI scintillator. Due to an aluminum faceplate on the CsI crystals holding them in place, the light output was constrained to a 4 mm diameter circle causing dark regions in between each circle of signal. To convert this to a more usable format, the number of counts in each pixel within each circular region was summed together into one data point. A comparison of the raw and reformatted data can be seen in Figs. 2(c) and 2(d).

B. GEANT4 simulations

In order to analyze the data obtained from the crystal array, it is imperative to know how gamma rays will interact with CsI at various energies. Several 3D simulations were carried out in GEANT4[27] with various monoenergetic photon beams irradiating a slab of CsI, as shown in Fig. 2(e), to generate response curves for the photon energies relevant to this experiment. For this work, it was necessary to carry out 3D simulations due to significant amounts of side scatter and electron cascading that took place within the crystal array. Two dimensions were necessary to account for scattering and energy transfer between neighboring CsI crystals, and the third dimension was necessary to properly capture the geometry of the array so that light yield calculated by the simulations could be accurately compared to data. The incident photon energy in the simulations was varied from 0.1 MeV to 500 MeV with finer steps at low energy and larger steps at high energy. The lower limit was chosen because photons less than 0.1 MeV would not contribute any significant signal through the 9 mm thick steel detector housing. The simulations were stopped at 500 MeV as calculations indicate that the interaction would produce photons above this threshold in negligible quantities, well below the noise floor of the measurement.
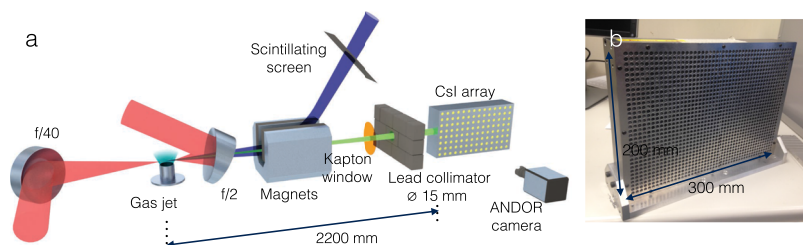

FIG. 1. (a) Experimental setup of the Compton scattering experiment, including the γ-ray spectrometer. (b) Photograph of the CsI scintillator array used as the detector.
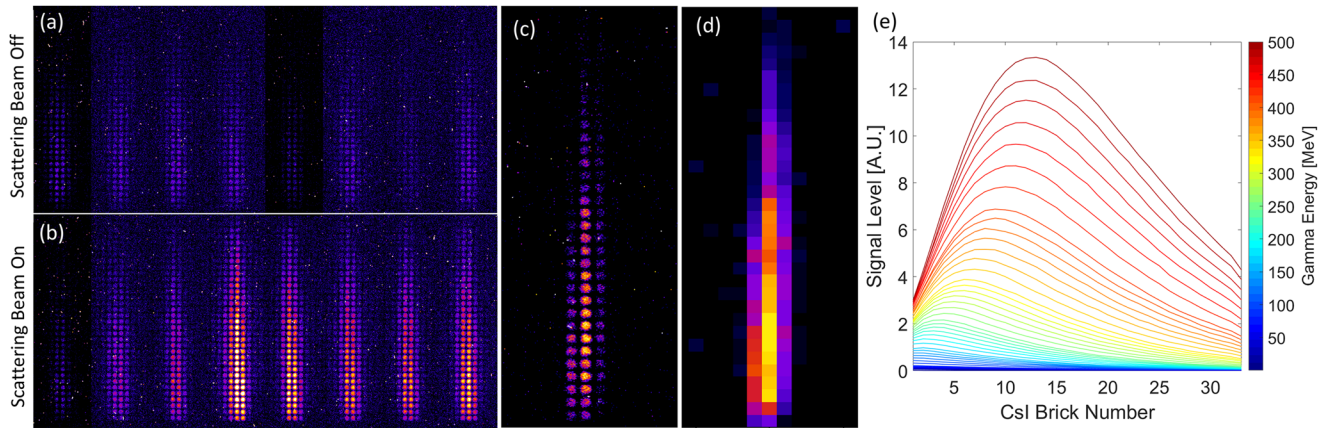
FIG. 2. (a) CsI scintillator raw data without the counter-propagating scattering beam. The signal is due to bremsstrahlung. (b) Raw data with the scattering beam on. The increase is due to gamma ray production through inverse Compton scattering of the electron beam with the counter-propagating $f/2$ beam. (c) Single image of the CsI detector array obtained by imaging the scintillator with a camera. (d) The processed image with the individual pixels in each circle summed for spectral analysis. (e) Energy deposition curves of a monoenergetic photon beam impinging on a CsI detector array from 47 different Monte Carlo simulations performed in GEANT4.

C. Image processing

The first step in analyzing the data files before the pixels were summed together was to perform a background subtraction. In these data, there are two types of background that must be accounted for: the dark noise of the camera that provides a signal level of roughly 100 ± 2 counts even when the laser is turned off and the background bremsstrahlung signal that appears when the scattering beam is turned off, but electrons are still produced. This signal is likely the result of stray electrons hitting the spectrometer magnets, shielding, or chamber walls. These two types of background signals can be seen in Figs. 3(a) and 3(b).

To account for the dark noise of the camera, the region of the image containing the CsI signal was cropped out and a background map was created from the remaining part of the image. This was done by performing a linear fit across each column of the remaining image and smoothing the result to generate a 1024×1024 "heatmap" of the background so that areas of slightly higher or lower dark noise were properly accounted for. This dark noise background subtraction was performed for each of the data shots and background bremsstrahlung shots.

Despite significant shielding with lead bricks, the spectrometer camera was still susceptible to stray electron and gamma hits causing occasional high peaks of signal ("hot pixels") across the image. Taking the Laplacian of the image after background subtraction enhanced the contrast between the hot pixels and the remainder of the image due to the large difference in the signal level compared to neighboring pixels. The hot pixels were selected by identifying outlier pixels that had counts significantly higher or lower than the standard deviation of the row. These outliers were removed and replaced with an average of the surrounding points such that hard events occurring in the signal region were blended with the signal and background events were blended with the background.

Lastly, it was important to account for the bremsstrahlung signal generated in addition to the gamma ray photons produced through the inverse Compton scattering interaction. The level of this background varied from shot to shot, as shown in Fig. 2(a). Since it was impossible to know the exact level of non-inverse Compton gamma photons that contributed to the signal on every shot, this variable background was a source of error in the spectrum calculations. Further discussion of how the background was accounted for in the calculations is covered in Sec. II E.
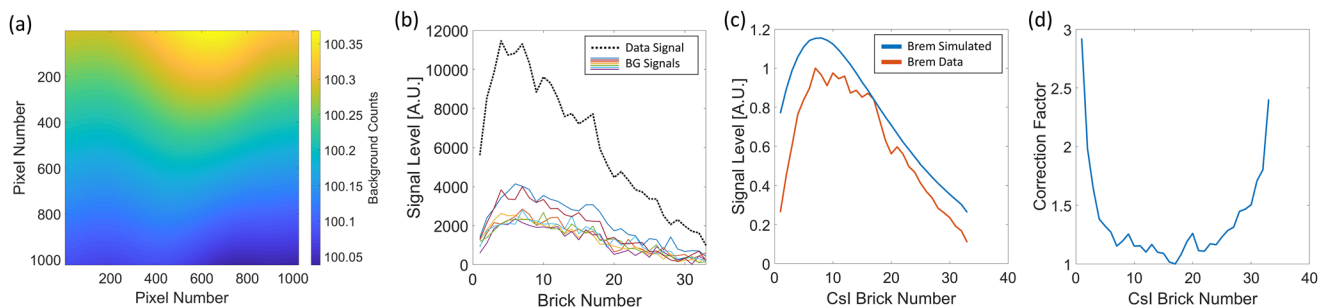
FIG. 3. (a) A "heatmap" of the dark noise background that was calculated and subtracted from each shot. (b) Seven different bremsstrahlung background curves plotted below an example data signal. The seven curves were subtracted from each data signal in the analysis. (c) Comparison of the theoretical bremsstrahlung signal to the actual bremsstrahlung data obtained during the experiment. The background data are normalized to the maximum value and the simulated background is normalized to the point of first overlap with the data. (d) Camera correction factor generated by dividing the theoretical signal by the actual signal.

D. Correction factor

During the experiment, calibration shots were performed by colliding the electron beam with a 9 mm thick piece of lead to measure the CsI signal resulting from a bremsstrahlung interaction. By comparing this signal to a simulated bremsstrahlung signal, it was possible to confirm the reliability of the detector and determine if the CsI detector system responded as expected to the gamma ray beam. The signal comparison between the data and simulation can be seen in Fig. 3(c). The curves in this figure were generated by summing the signal of the CsI crystals down the columns to compare the total signal generated from the experiment and simulation.

The theoretical bremsstrahlung signal was generated in GEANT4 by simulating the collision of an electron beam with an energy spectrum typical of the experiment with a 9 mm thick piece of lead. The resulting gamma ray beam interacted with a simulated detector to generate a CsI signal that could be compared with the experimental signal. This comparison required the assumption that the detector response to bremsstrahlung radiation was very similar in shape for slightly varying electron spectra; this was verified through simulation and the experimental data. The difference between the actual signal and the theoretical signal indicated a problem with the detector, most notably in the first few and last few crystals. The discrepancy between the measured bremsstrahlung signal and the theoretical signal along with verification of a consistent CsI signal resulted in the creation of a single "camera correction" curve to be applied to all the data during the analysis; this correction is shown in Fig. 3(d).

Along with correcting for the low light yield of the first and last few crystals, likely caused by poor crystal quality or inadequate capture of the CsI fluorescence due to the optics used for the camera (vignetting), it was important to correct for the non-uniformity of the crystal light yield. This ensured that the calculations were performed with a more accurately represented signal curve. While the correction factor accounted for the shape of the signal along with some of the inherent non-uniformity, it was not complete and applying a smooth fit to the noisy data to obtain an ideal signal level could fully account for the residual noise. The simulated signal in Fig. 3(c) and the detector response curves in Fig. 2(e) indicate that the CsI signal should not vary from one crystal to the next as significantly as the experimental data indicate. The non-uniformity of the crystal light output was a source of error in the spectral calculations as the noise allowed for several different best-fit lines to the same data.

For this work, we defined a few different parameters to aid in describing the quality of the fit. We define the *experimental error* as the standard deviation of the difference between the measured data S_i and the smooth best fit curve f_i, normalized by the summed signal level of the best fit curve,

$$\text{Experimental Error} = \frac{\sigma(S_i - f_i)}{\sum_i f_i}. \tag{1}$$

This *experimental error* is a measure of the inherent error of the detector and will be used later as a benchmark for the error of the calculated signal to the measured signal. Figure 4(a) shows an example of the *experimental error* calculation with the red arrows indicating the amplitude difference between the data and the best fit (ideal signal). The best fit to the data was calculated by performing 6th, 7th, and 8th degree polynomial fits to the data and choosing the curve with the best fit quality.
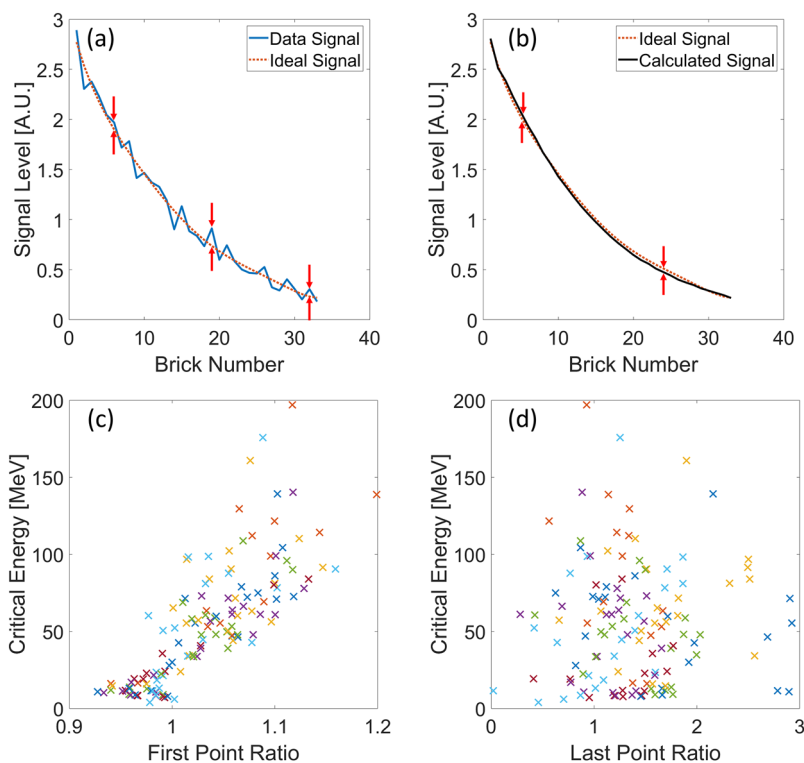

FIG. 4. (a) Comparison between the data signal and the ideal signal obtained by a best fit. The red arrows show some of the amplitude differences that were measured in calculating the *experimental error*. (b) Comparison between the calculated signal and the ideal signal for the same shot as (a). The difference between the two signals is used to calculate the *relative error*. (c) Relationship between the critical energy and the ratio of the last data point and last point of the calculated signal. (d) Relationship between the critical energy and the ratio of the first data point to the first point of the calculated signal. Each color "×" represents the 7 background subtractions of a single shot.

E. Iterative calculations

An algorithm was written to calculate the input spectrum that would match the data after simulating its interaction with the CsI array in GEANT4. The algorithm is similar to the YOGI code[28,29] in which the spectrum is calculated by introducing perturbations to an assumed exponential shape and checking the result of those perturbations against the data curve. The form of the exponential spectrum used in this algorithm is

$$\frac{dN}{dE} = A \times E^{-2/3} \times e^{-\frac{E}{E_c}}. \tag{2}$$

This form was the best fit equation to a spectrum produced by a simulated inverse nonlinear Compton scattering interaction.[18,21] In this equation, A is the amplitude of the spectrum, E is the photon energy, and E_{crit} is the characteristic energy of the spectrum with 49% of the photon energy radiated below E_c and the mean photon energy being $E_c/3$.

A single gamma ray of energy E incident on the scintillator array will generate a response $\rho_i(E)$, where i denotes the ith element in the array. The response of the CsI scintillator to deposited energy is linear, and so for distribution of photons, the total signal measured on the scintillator array will be $S_i = \int_0^\infty \rho_i(E) f(E) dE$, where $f(E)dE$ is the number of photons with energies in the range E to $E + dE$.

Using GEANT4, we calculated responses for a series of photon distributions $f_{calc}(E, E_c) = (dN/dE)/A$, given by Eq. (2), over a range of values of E_{crit}^j, where j is the jth calculated spectrum. This yielded a series of simulated scintillator array signals,

$$\Sigma_i(E_c^j) = \int_0^\infty \rho_{calc}^i(E) f_{calc}(E, E_{crit}^j) dE$$
$$= \int_0^\infty \rho_{calc}^i(E) E^{-2/3} \exp\left(-\frac{E}{E_c^j}\right) dE, \tag{3}$$

where $\rho_{calc}^i(E)$ is the simulated response function, i.e., the signal calculated in the simulated array by GEANT4 for a photon of energy E.
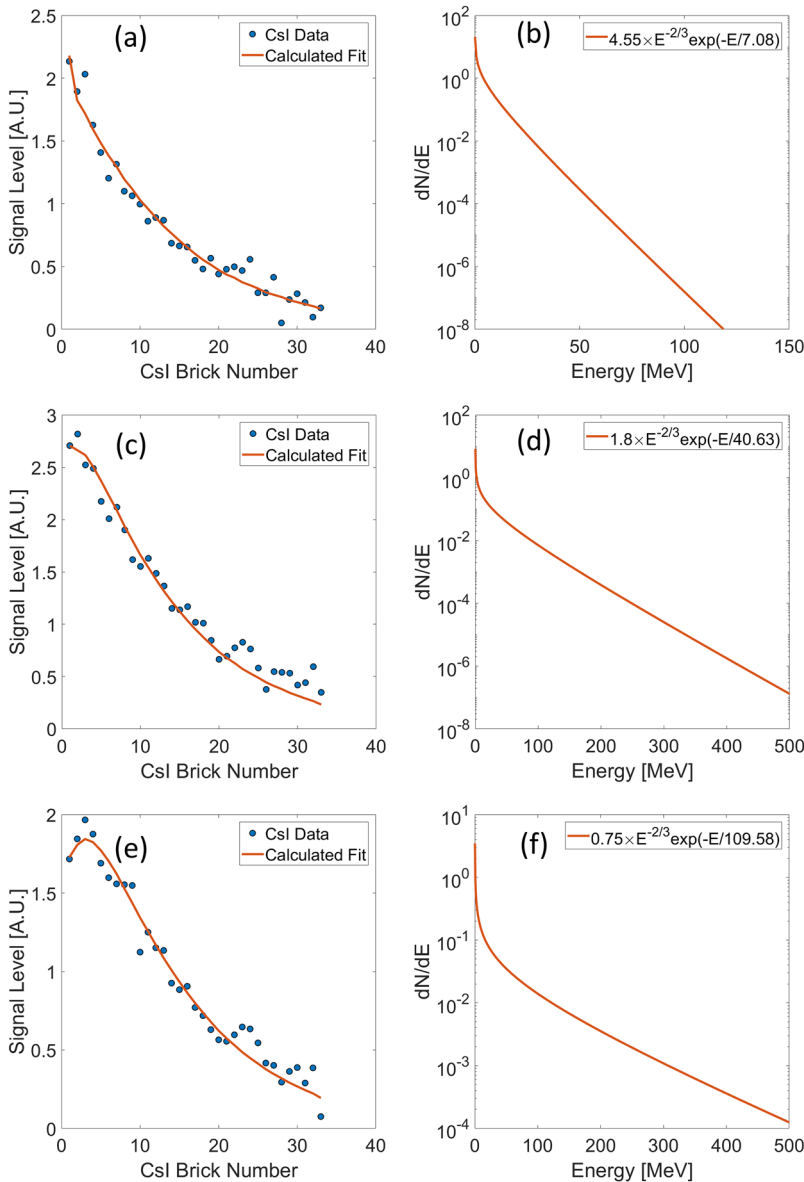

FIG. 5. Data and calculated fit plotted with corresponding spectra. The data obtained from the CsI detector are marked with the blue dots and the calculated fit is plotted as the solid line among the dots. [(a) and (b)] Example of a low critical energy fit and spectrum of $E_{crit} = 7.08$ MeV. [(c) and (d)] Example of a moderate critical energy fit and spectrum with $E_{crit} = 40.63$ MeV. [(e) and (f)] Example of a high critical energy fit and spectrum with $E_{crit} = 109.58$ MeV.

TABLE I. Table showing the values returned by running the fitting algorithm to the seven background subtracted data curves. The results show that the fit with the highest R^2 does not always correspond to the fit with the highest first point ratio (FPR), which is why both needed to be considered in choosing the background that resulted in the best fit. A and E_c are the amplitude and critical energy of the fitting spectrum given in Eq. (2).

Parameter	BG 1	BG 2	BG 3	BG 4	BG 5	BG 6	BG 7
R^2	0.997	0.992	0.986	0.989	0.988	0.993	0.969
FPR	0.991	1.003	1.035	1.030	0.977	0.991	1.015
E_c (MeV)	21.22	52.26	98.63	44.71	60.12	50.61	33.84
A	2.11	1.43	0.98	1.68	1.33	1.47	1.62

For the iterative calculation of the experimental spectrum, starting with a guessed spectrum $f_{calc}(E, E_c^0)$, the measured signal for a particular shot S_i was compared with $\Sigma_i(E_c^0)$. A new guessed spectrum was calculated by adding a random perturbation to A_j and E_{crit}^j to generate new spectra with

$A_{j+1} = A_j + \delta A$, $E_c^{j+1} = E_c^j + \delta E_c$ for a number of perturbations in a generation j, and the quality of the fit between the data and the calculated signal was characterized by the R^2 value,

$$R^2 = 1 - \frac{\sum_i (S_i - \Sigma_i)^2}{\sum_i (S_i - \bar{S}_i)^2} , \qquad (4)$$

where $\bar{S}_i$ is the average of S_i. The values A_{j+1} and E_c^{j+1} corresponding to the largest R^2 value for the different perturbations in the generation were then taken as the starting point for the next iteration, and when the algorithm converged, the spectrum $A_{j+1} E^{-2/3} \exp(-\frac{E}{E_c^{j+1}})$ was taken to best represent the real photon spectrum.

Similar to the *experimental error*, we define the *calculated error* as

$$\text{Calculated Error} = \frac{\sigma(\Sigma_i - f_i|}{\sum_i f_i} , \qquad (5)$$

as illustrated in Fig. 4(b). The calculated signal comes from the iterative perturbation method described previously, and the ideal signal is the same signal as listed in Eq. (1).
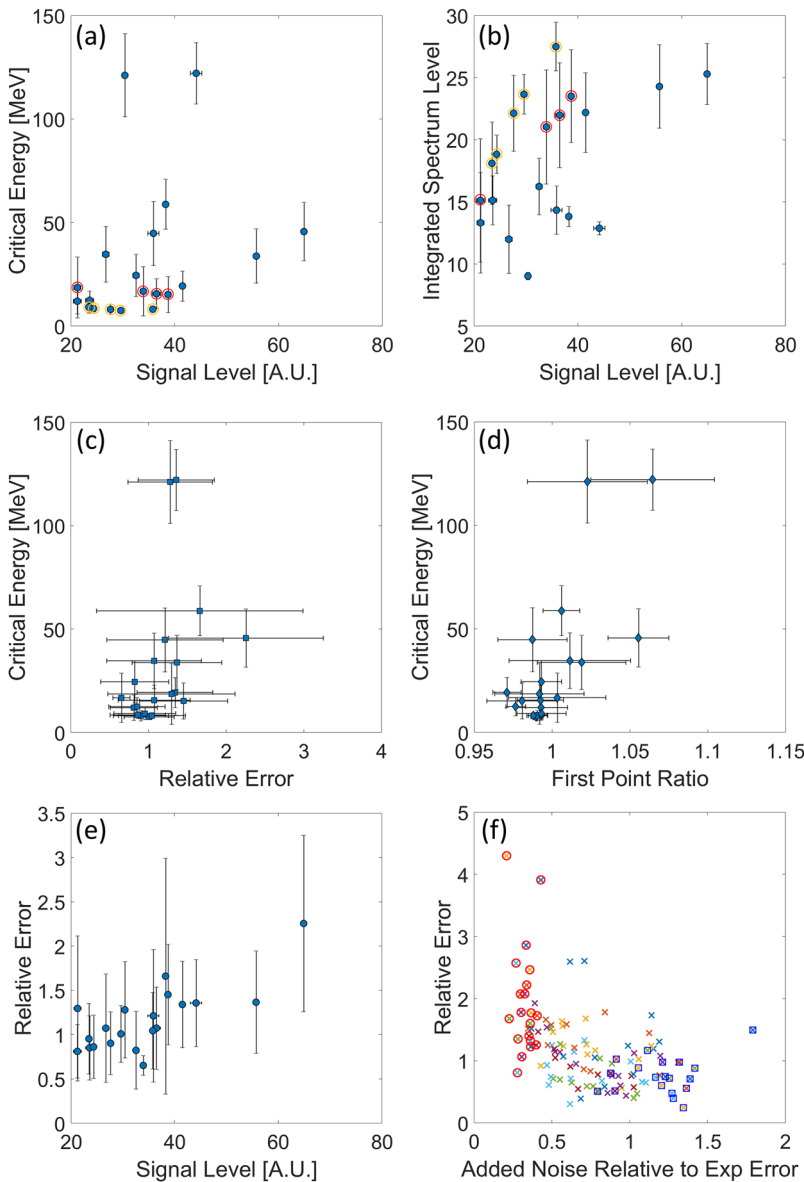

FIG. 6. Measurements of various trends across 20 shots. (a) The integrated signal level on the CsI detector plotted against the measured critical energy. (b) shows the relationship between the CsI detector signal level and the area under the curve of the calculated spectrum. (c) shows that there is no relationship between the relative error (defined in Sec. II E) and the critical energy. (d) The relationship between the first point ratio and the critical energy after the correct background was subtracted. (e) Relative error plotted against the detector signal level showing a slight positive trend. (f) Relative error plotted against the added noise. The minimum added noise and maximum added noise are highlighted with red circles and blue squares, respectively.

Characterizing the fit of the calculated signal this way is useful because it can be compared directly to the inherit error of the detector through the *experimental error*. An example of the calculated signal with the raw data and the calculated spectrum can be seen in Figs. 5(a)–5(f).

As mentioned previously, determining the proper background subtraction was challenging in this work as it had a significant effect on the resulting fit and spectrum. Starting with a [1 × 33] vector of data, *s*, having the correction factor applied, seven different background shots, *b*, were subtracted such that *s*′ is a matrix derived from the concatenation of the vectors *s* − *b* of size [7 × 33]. Now there are seven different data curves for each shot, each with its own potential background subtraction. The fitting algorithm was run to calculate the critical energy (E_{crit}), amplitude (*A*), fit quality (R^2), and ratio between the first point of the data and the first point of the fit for each of the seven options. Seven background shots were chosen as they were consecutive shots that were representative of the potential background produced by the wakefield beam only. The CsI signal of these seven shots can be found in Fig. 3 of the work of Cole *et al.*[21] (A cluster of four points with similar $Q\langle\gamma^2\rangle$ and CsI signal can be seen in Fig. 3 of the work of Cole *et al.*[21] 3 of these points were not included in the analysis to give a more conservative estimate of the background variation.) An example of these numbers for a data shot is shown in Table I. The relationship between the first point of the data and the fit is important as the fit quality of the first few points has a much higher effect on the calculated critical energy than the last few points. Figure 4(c) shows that when the ratio of the first point of the data to the first point of the calculated signal is greater than 1, the algorithm over-estimates the critical energy and when it is less than 1, the critical energy is under-estimated. Figure 4(d) shows that the fit quality of the last point does not affect the critical energy.

To define which background subtraction was the "correct" subtraction, the R^2 value was averaged with the first point ratio for each of the seven calculated signals and the result closest to unity was chosen as the proper background subtraction. Averaging the two values together proved to be the best way to equally weigh each of the two measurements. This method took into account both the quality of the fit and accuracy of the first point fit as it was possible to have background subtraction with a high fit quality overall but poor fit on the first point resulting in a heavily over- or under-estimated critical energy.

Upon determining the correct background subtraction for each shot, a noise analysis was performed to determine the sensitivity of the critical energy calculations to noisy data. For each shot, the *experimental error* was used as the amplitude metric and random noise was added to each bin of the ideal signal ranging from ½ to 2× the *experimental error*. Once new signal was generated with the synthetic noise, an ideal signal was found for each of the new signal curves and the fitting algorithm was rerun. Since the correct background was already chosen for each shot, the error due to the synthetic noise indicated the error of the original critical energy calculation as this depended on the ideal signal that was generated by performing a best-fit to the data. The results of the noise analysis can be seen in Fig. 6.

III. RESULTS

Comparing the *calculated error* to the *experimental error* is a good way to quantify the quality of the fit with respect to the original data. To determine how well the calculated signal fits the data, the *relative error* is

$$\text{Relative Error} = \frac{\sigma(\Sigma_i - f_i)}{\sigma(S_i - f_i)}. \tag{6}$$

The integral of the ideal signal (from the denominator) cancels when these two errors are divided by one another.

Figure 6 compares the critical energy, detector signal level (the summation of the "counts" in each crystal), integrated spectrum level, and fit quality parameters to one another. In (a) and (b) of the figure are plots that describe the physics of the inverse Compton scattering interaction and in (c)–(f) are plots that describe the success of the iterative algorithm. Figure 6(a) shows the critical energy plotted against the signal level of the detector. There appears to be a very weak positive trend between the CsI signal level and the calculated critical energy if a few of the higher, outlier signals are ignored. This is somewhat to be expected as a more successful overlap of the electron beam with the scattering laser should produce more photons and higher energy photons. If the trend were stronger, it would indicate that the number of electrons interacting with the laser pulse on each shot remained constant. The rather weak trend indicates that the number of electrons scattered by the laser on each shot was not constant, likely due to the charge variability in the electron beam and fluctuations in the laser-electron beam overlap. In Fig. 6(b), the relationship between the integrated signal on the detector and the integrated reconstructed spectrum is compared. If the critical energy was the same for all spectra, all the points on this plot would lie on a straight line. The increasing trend is expected, however, because higher energy photons deposit more signals into the detector than lower energy photons [see Fig. 2(e)]. For shots with the same critical energy, there is a direct, linear relationship between the number of photons and the CsI signal level that can be extracted. The highlighted shots in Figs. 6(a) and 6(b) show some of these shots with a similar critical energy.

The trends shown in Figs. 6(c)–6(f) are more telling of the fitting algorithm than the physics of the interaction. In Fig. 6(c), the critical energy is plotted against the first point ratio for the noise analysis data as opposed to the background subtracted data as is the case with Fig. 4(a). This now shows that the relationship between the first point and the critical energy is much weaker and that most of the points are very close to unity. This indicates that the critical energy measurement is more trustworthy and the over- or under-estimation is within a reasonable error. The plot in Fig. 6(d) shows that there is no relationship between the critical energy and the relative error. This is desirable as a relationship between the energy of the photons and the fit quality would imply that there were errors with the simulations. The plot indicates that over 75% of the points have a relative error of less than 2.0, indicating a strong fit quality among most of the shots. Plot (e) shows that there is a slightly positive relationship between the relative error and the detector signal level which is unexpected because the relative error is independent of the signal level, as seen in Eq. (6). Further analysis revealed that the result of

this slight positive trend is due to the positive trend that exists between the signal level and the numerator of the *calculated error* and the lack of a positive trend between the numerator of the *experimental error* and the signal level. Lastly, plot (f) shows the relationship between the relative error and the added noise. As expected, the relative error decreases with increasing noise because higher noise means a higher *experimental error*, which is the denominator of Eq. (6). The highlighted red and blue points show the minimum and maximum added noise, respectively. As expected, the minimum noise resulted in higher discrepancies between the calculated fit quality and the ideal signal.

IV. CONCLUSIONS

In conclusion, we developed a CsI gamma ray spectrometer by placing an array of CsI crystals parallel to the gamma beam propagation direction in order to measure the penetration depth. The measurements of CsI scintillation were made with the counter-propagating beam turned on and off, as shown in Fig. 2. The figure shows that on average, the CsI bricks produced a higher light yield when the scattering beam was turned on indicating that the counter-propagating laser pulse caused the creation of high energy gamma rays. Since the increase in signal above the background bremsstrahlung signal was the result of only turning on the scattering beam, we are confident that the source of gamma rays is from inverse Compton scattering. With many of the shots producing spectra with critical energies higher than 30 MeV, this represents highest energy gamma rays produced through inverse Compton scattering on an all-optical source to date.

We were able to use this detector as a spectrometer by perturbing an assumed exponential spectrum and using GEANT4 simulations to match the detector response to the data.[30,31] The resulting fit between the data and the signal produced by calculated spectra was overall very good with the majority of the shots having a lower error than the inherent error of the CsI fluorescence. With GEANT4 simulations performed in advance, this detector setup along with the algorithm could be implemented in future experiments as a gamma ray spectrometer capable of producing a spectrum on a shot-by-shot basis. To improve the detector design, it would be beneficial to change the 9 mm thick steel side plate to a thinner, lower-Z material to mitigate the absorption of gamma rays in the housing. It would also be helpful to remove the faceplate of the detector that restricts the fluorescence to circular holes so that each crystal's fluorescence can be captured entirely.

[1] C. Geddes, C. Toth, J. Van Tilborg, E. Esarey, C. Schroeder, D. Bruhwiler, C. Nieter, J. Cary, and W. Leemans, "High-quality electron beams from a laser wakefield accelerator using plasma-channel guiding," Nature **431**(7008), 538–541 (2004).

[2] J. Faure, Y. Glinec, A. Pukhov, S. Kiselev, S. Gordienko, E. Lefebvre, J.-P. Rousseau, F. Burgy, and V. Malka, "A laser-plasma accelerator producing monoenergetic electron beams," Nature **431**(7008), 541–544 (2004).

[3] S. Mangles, C. Murphy, Z. Najmudin, A. Thomas, J. Collier, A. Dangor, E. Divall, P. Foster, J. Gallacher, C. Hooker, D. Jaroszynski, A. Langley, W. Mori, P. Norreys, F. Tsung, R. Viskup, B. Walton, and K. Krushelnick, "Monoenergetic beams of relativistic electrons from intense laser-plasma interactions," Nature **431**(7008), 535–538 (2004).

[4] F. Albert and A. G. Thomas, "Applications of laser wakefield accelerator-based light sources," Plasma Phys. Controlled Fusion **58**(10), 103001 (2016).

[5] P. Lale, "The examination of internal tissues, using gamma-ray scatter with a possible extension to megavoltage radiography," Phys. Med. Biol. **4**(2), 159 (1959).

[6] R. Clarke and G. Van Dyk, "Compton-scattered gamma rays in diagnostic radiography," in Medical Radioisotope Scintigraphy. VI. Proceedings of a Symposium on Medical Radioisotope Scintigraphy, 1969.

[7] K. T. Phuoc, S. Corde, C. Thaury, V. Malka, A. Tafzi, J.-P. Goddet, R. C. Shah, S. Sebban, and A. Rousse, "All-optical Compton gamma-ray source," Nat. Photon. **6**, 308–311 (2012).

[8] S. Chen, N. Powers, I. Ghebregziabher, C. Maharjan, C. Liu, G. Golovin, S. Banerjee, J. Zhang, N. Cunningham, A. Moorti *et al.*, "MeV-energy x rays from inverse compton scattering with laser-wakefield accelerated electrons," Phys. Rev. Lett. **110**(15), 155003 (2013).

[9] G. Sarri, D. Corvan, W. Schumaker, J. Cole, A. Di Piazza, H. Ahmed, C. Harvey, C. H. Keitel, K. Krushelnick, S. Mangles *et al.*, "Ultrahigh brilliance multi-MeV γ-ray beams from nonlinear relativistic Thomson scattering," Phys. Rev. Lett. **113**(22), 224801 (2014).

[10] W. Yan, C. Fruhling, G. Golovin, D. Haden, J. Luo, P. Zhang, B. Zhao, J. Zhang, C. Liu, M. Chen, S. Chen, S. Banerjee, and D. Umstadter, "High-order multiphoton Thomson scattering," Nat. Photonics **11**, 514 (2017).

[11] V. Malka, J. Faure, Y. A. Gauduel, E. Lefebvre, A. Rousse, and K. T. Phuoc, "Principles and applications of compact laser-plasma accelerators," Nat. Phys. **4**, 447–453 (2008).

[12] T. Fuchs, H. Szymanowski, U. Oelfke, Y. Glinec, C. Rechatin, J. Faure, and V. Malka, "Treatment planning for laser-accelerated very-high energy electrons," Phys. Med. Biol. **54**(11), 3315 (2009).

[13] Y. Glinec, J. Faure, L. Le Dain, S. Darbon, T. Hosokai, J. Santos, E. Lefebvre, J.-P. Rousseau, F. Burgy, B. Mercier *et al.*, "High-resolution γ-ray radiography produced by a laser-plasma driven electron source," Phys. Rev. Lett. **94**(2), 025003 (2005).

[14] F. Albert, S. Anderson, G. Anderson, S. Betts, D. Gibson, C. Hagmann, J. Hall, M. Johnson, M. Messerly, V. Semenov, M. Shverdin, A. Tremaine, F. Hartemann, C. Siders, D. McNabb, and C. Barty, "Isotope-specific detection of low-density materials with laser-based monoenergetic gamma-rays," Opt. Lett. **35**(3), 354–356 (2010).

[15] R. T. Klann, J. Shergur, and G. Mattesich, "Current state of commercial radiation detection equipment for homeland security applications," Nucl. Technol. **168**(1), 79–88 (2009).

[16] C. Moss, C. Hollas, G. McKinney, and W. Myers, "Comparison of active interrogation techniques," in IEEE Nuclear Science Symposium Conference Record (IEEE, 2005), Vol. 1, pp. 329–332.

[17] A. G. R. Thomas, C. P. Ridgers, S. S. Bulanov, B. J. Griffin, and S. P. D. Mangles, "Strong radiation-damping effects in a gamma-ray source generated by the interaction of a high-intensity laser with a wakefield-accelerated electron beam," Phys. Rev. X **2**, 041004 (2012).

[18] T. G. Blackburn, C. P. Ridgers, J. G. Kirk, and A. R. Bell, "Quantum radiation reaction in laser-electron-beam collisions," Phys. Rev. Lett. **112**, 015001 (2014).

[19] E. Nerush, I. Kostyukov, A. Fedotov, N. Narozhny, N. Elkina, and H. Ruhl, "Laser field absorption in self-generated electron-positron pair plasma," Phys. Rev. Lett. **106**, 035001 (2011).

[20]N. Elkina, A. Fedotov, I. Kostyukov, M. Legkov, N. Narozhny, E. Nerush, and H. Ruhl, "QED cascades induced by circularly polarized laser fields," Phys. Rev. Accel. Beams **14**, 054401 (2011).

[21]J. M. Cole, K. T. Behm, E. Gerstmayr, T. G. Blackburn, J. C. Wood, C. D. Baird, M. J. Duff, C. Harvey, A. Ilderton, A. S. Joglekar, K. Krushelnick, S. Kuschel, M. Marklund, P. McKenna, C. D. Murphy, K. Poder, C. P. Ridgers, G. M. Samarin, G. Sarri, D. R. Symes, A. G. R. Thomas, J. Warwick, M. Zepf, Z. Najmudin, and S. P. D. Mangles, "Experimental evidence of radiation reaction in the collision of a high-intensity laser pulse with a laser-wakefield accelerated electron beam," Phys. Rev. X **8**, 011020 (2018).

[22]K. Poder, M. Tamburini, G. Sarri, A. Di Piazza, S. Kuschel, C. D. Baird, K. Behm, S. Bohlen, J. M. Cole, D. J. Corvan, M. Duff, E. Gerstmayr, C. H. Keitel, K. Krushelnick, S. P. D. Mangles, P. McKenna, C. D. Murphy, Z. Najmudin, C. P. Ridgers, G. M. Samarin, D. R. Symes, A. G. R. Thomas, J. Warwick, and M. Zepf, "Experimental signatures of the quantum nature of radiation reaction in the field of an ultraintense laser," Phys. Rev. X **8**, 031004 (2018).

[23]G. F. Knoll, *Radiation Detection and Measurement*, 4th ed. (Wiley, New York, NY, 2010).

[24]T. Ypsilantis and J. Seguinot, "Theory of ring imaging Cherenkov counters," Nucl. Instrum. Methods Phys. Res., Sect. A **343**(1), 30–51 (1994).

[25]V. Schönfelder and G. Kanbach, *Imaging through Compton Scattering and Pair Creation* (Springer New York, New York, NY, 2013), pp. 225–242.

[26]D. J. Corvan, G. Sarri, and M. Zepf, "Design of a compact spectrometer for high-flux MeV gamma-ray beams," Rev. Sci. Instrum. **85**(6), 065119 (2014).

[27]S. Agostinelli, J. Allison, K. Amako, J. Apostolakis, H. Araujo, P. Arce, M. Asai, D. Axen, S. Banerjee, G. Barrand *et al.*, "Geant4—A simulation toolkit," Nucl. Instrum. Methods Phys. Res., Sect. A **506**, 250 (2003).

[28]G. Carlson, D. Fehl, and L. Lorence, "A differential absorption spectrometer for determining flash x-ray spectra," Nucl. Instrum. Methods Phys. Res., Sect. B **62**(2), 264–274 (1991).

[29]S. G. Gorbics and N. Pereira, "Differential absorption spectrometer for pulsed bremsstrahlung," Rev. Sci. Instrum. **64**(7), 1835–1840 (1993).

[30]J. H. Jeon, K. Nakajima, H. T. Kim, Y. J. Rhee, V. B. Pathak, M. H. Cho, J. H. Shin, B. J. Yoo, C. Hojbota, S. H. Jo, K. W. Shin, J. H. Sung, S. K. Lee, B. I. Cho, I. W. Choi, and C. H. Nam, "A broadband gamma-ray spectrometry using novel unfolding algorithms for characterization of laser wakefield-generated betatron radiation," Rev. Sci. Instrum. **86**(12), 123116 (2015).

[31]J. H. Jeon, K. Nakajima, H. T. Kim, Y. J. Rhee, V. B. Pathak, M. H. Cho, J. H. Shin, B. J. Yoo, S. H. Jo, K. W. Shin, C. Hojbota, L. J. Bae, J. Jung, M. S. Cho, J. H. Sung, S. K. Lee, B. I. Cho, I. W. Choi, and C. H. Nam, "Measurement of angularly dependent spectra of betatron gamma-rays from a laser plasma accelerator with quadrant-sectored range filters," Phys. Plasmas **23**(7), 073105 (2016).